

Optical breakdown in transparent media with adjustable axial length and location

Ilya Toytman,^{1,*} Dmitri Simanovski,¹ and Daniel Palanker^{1,2}

¹Hansen Experimental Physics Laboratory, Stanford University, 452 Lomita Mall,
Stanford, CA 94305 USA

²Department of Ophthalmology, Stanford University School of Medicine, 300 Pasteur Drive,
Stanford, CA 94305 USA

*itoytman@stanford.edu

Abstract: We demonstrate a highly elongated (aspect ratio over 500:1) optical breakdown in water produced by a single pulse of a picosecond laser focused with a combination of an axicon and a lens. Locations of the proximal and distal ends of the breakdown region can be adjusted by modifying radial intensity distribution of the incident beam with an amplitude mask. Using Fresnel diffraction theory we derive a transmission profile of the amplitude mask to create a uniform axial intensity distribution in the breakdown zone. Experimentally observed dynamics of the bubbles obtained with the designed mask is in agreement with the theoretical model. A system producing an adjustable cylindrical breakdown can be applied to fast linear or planar dissection of transparent materials. It might be useful for ophthalmic surgical applications including cataract surgery and crystalline lens softening.

©2010 Optical Society of America

OCIS codes: (140.3440) Laser-induced breakdown; (170.4460) Ophthalmic optics and devices; (260.7120) Ultrafast phenomena.

References and links

1. Z. Nagy, A. Takacs, T. Filkorn, and M. Sarayba, "Initial clinical evaluation of an intraocular femtosecond laser in cataract surgery," *J. Refract. Surg.* **25**(12), 1053–1060 (2009).
2. S. Schumacher, U. Oberheide, M. Fromm, T. Ripken, W. Ertmer, G. Gerten, A. Wegener, and H. Lubatschowski, "Femtosecond laser induced flexibility change of human donor lenses," *Vision Res.* **49**(14), 1853–1859 (2009).
3. U. K. Tirlapur, and K. König, "Targeted transfection by femtosecond laser," *Nature* **418**(6895), 290–291 (2002).
4. K. König, I. Riemann, and W. Fritzsche, "Nanodissection of human chromosomes with near-infrared femtosecond laser pulses," *Opt. Lett.* **26**(11), 819–821 (2001).
5. Z. Nagy, J. F. Doane, D. S. Durrie, M. C. Kraff, R. L. Lindstrom, S. G. Slade, and R. F. Steinert, "Use of the femtosecond laser system in cataract surgery" presented at the American Academy of Ophthalmology Annual Meeting, San Francisco, CA, USA, 24–27 October 2009.
6. J. Durmin, "Exact solutions for nondiffracting beams. I. Scalar theory," *J. Opt. Soc. Am. A* **4**, 651–654 (1987).
7. J. H. McLeod, "The Axicon: A New Type of Optical Element," *J. Opt. Soc. Am.* **44**, 592–592 (1954).
8. X. Tsampoula, V. Garcés-Chávez, M. Comrie, D. J. Stevenson, B. Agate, C. T. A. Brown, F. Gunn-Moore, and K. Dholakia, "Femtosecond cellular transfection using a nondiffracting light beam," *Appl. Phys. Lett.* **91**, 053902 (2007).
9. Y. Matsuoka, Y. Kizuka, and T. Inoue, "The characteristics of laser micro drilling using a Bessel beam," *Appl. Phys., A Mater. Sci. Process.* **84**, 423–430 (2006).
10. O. Brzobohatý, T. Cizmár, and P. Zemánek, "High quality quasi-Bessel beam generated by round-tip axicon," *Opt. Express* **16**(17), 12688–12700 (2008).
11. T. Cizmár, and K. Dholakia, "Tunable Bessel light modes: engineering the axial propagation," *Opt. Express* **17**(18), 15558–15570 (2009).
12. M. K. Bhuyan, F. Courvoisier, P.-A. Lacourt, M. Jacquot, L. Furfaro, M. J. Withford, and J. M. Dudley, "High aspect ratio taper-free microchannel fabrication using femtosecond Bessel beams," *Opt. Express* **18**(2), 566–574 (2010).
13. J. Durmin, J. J. Miceli, Jr., and J. H. Eberly, "Diffraction-free beams," *Phys. Rev. Lett.* **58**(15), 1499–1501 (1987).
14. Y. Chen, J. Pu, and X. Liu, "Axial intensity distribution of lens axicon illuminated by Gaussian-Schell model beam," *Opt. Eng.* **46**, 018003 (2007).
15. S. R. Mishra, S. K. Tiwari, S. P. Ram, and S. C. Mehendale, "Generation of hollow conic beams using a metal axicon mirror," *Opt. Eng.* **46**, 084002 (2007).

16. A. Vasara, J. Turunen, and A. T. Friberg, "Realization of general nondiffracting beams with computer-generated holograms," *J. Opt. Soc. Am. A* **6**(11), 1748–1754 (1989).
17. A. J. Cox, and D. C. Dibble, "Nondiffracting beam from a spatially filtered Fabry-Perot resonator," *J. Opt. Soc. Am. A* **9**, 282–286 (1992).
18. M. Born, and E. Wolf, *Principles of Optics* (Pergamon, 1970).
19. K. Tsiglifis, and N. A. Pelekasis, "Nonlinear oscillations and collapse of elongated bubbles subject to weak viscous effects," *Phys. Fluids* **17**, 102101 (2005).
20. P. A. Quinto-Su, V. Venugopalan, and C.-D. Ohl, "Generation of laser-induced cavitation bubbles with a digital hologram," *Opt. Express* **16**(23), 18964–18969 (2008).
21. K. Y. Lim, P. A. Quinto-Su, E. Klaseboer, B. C. Khoo, V. Venugopalan, and C.-D. Ohl, "Nonspherical laser-induced cavitation bubbles," *Phys. Rev. E Stat. Nonlin. Soft Matter Phys.* **81**(1 Pt 2), 016308 (2010).
22. W. Lauterborn, and T. Kurz, "Physics of bubble oscillations," *Rep. Prog. Phys.* **73**, 106501 (2010).
23. E.-A. Brujan, and A. Vogel, "Stress wave emission and cavitation bubble dynamics by nanosecond optical breakdown in a tissue phantom," *J. Fluid Mech.* **558**, 281–308 (2006).
24. J. W. Goodman, *Introduction to Fourier Optics* (McGraw-Hill, 1996).
25. A. Vogel, N. Linz, S. Freidank, and G. Paltauf, "Femtosecond-laser-induced nanocavitation in water: implications for optical breakdown threshold and cell surgery," *Phys. Rev. Lett.* **100**(3), 038102 (2008).
26. F. H. Loesel, M. H. Niemz, J. F. Bille, and T. Juhasz, "Laser-induced optical breakdown on hard and soft tissues and its dependence on the pulse duration: experiment and model," *IEEE J. Quantum Electron.* **32**, 1717–1722 (1996).
27. Q. Feng, J. V. Moloney, A. C. Newell, E. M. Wright, K. Cook, P. K. Kennedy, D. X. Hammer, B. A. Rockwell, and C. R. Thompson, "Theory and simulation on the threshold of water breakdown induced by focused ultrashort laser pulses," *IEEE J. Quantum Electron.* **QE-33**, 127–137 (1997).
28. A. Vogel, J. Noack, K. Nahen, D. Theisen, S. Busch, U. Parltitz, D. X. Hammer, G. D. Noojin, B. A. Rockwell, and R. Birngruber, "Energy balance of optical breakdown in water at nanosecond to femtosecond time scales," *Appl. Phys. B* **68**, 271–280 (1999).
29. H. Sun, M. Han, M. H. Niemz, and J. F. Bille, "Femtosecond laser corneal ablation threshold: dependence on tissue depth and laser pulse width," *Lasers Surg. Med.* **39**(8), 654–658 (2007).
30. A. T. Friberg, "Stationary-phase analysis of generalized axicons," *J. Opt. Soc. Am. A* **13**, 743–750 (1996).
31. T. Čizmar, M. Mazilu, and K. Dholakia, "In situ wavefront correction and its application to micromanipulation," *Nat. Photonics* **4**, 388–394 (2010).
32. S. Schumacher, U. Oberheide, M. Fromm, W. Ertmer, G. Gerten, A. Wegener, and H. Lubatschowski, "Fslentotomy: first in vivo studies on rabbit eyes with a 100kHz laser system," *Proc. SPIE* **6844**, 68440V (2008).
33. R. J. Thomas, G. D. Noojin, D. J. Stolarski, R. T. Hall, C. P. Cain, C. A. Toth, and B. A. Rockwell, "A comparative study of retinal effects from continuous wave and femtosecond mode-locked lasers," *Lasers Surg. Med.* **31**(1), 9–17 (2002).
34. G. Schuele, M. Rumohr, G. Huettmann, and R. Brinkmann, "RPE damage thresholds and mechanisms for laser exposure in the microsecond-to-millisecond time regimen," *Invest. Ophthalmol. Vis. Sci.* **46**(2), 714–719 (2005).
35. C. Framme, G. Schuele, J. Roeder, D. Kracht, R. Birngruber, and R. Brinkmann, "Threshold determinations for selective retinal pigment epithelium damage with repetitive pulsed microsecond laser systems in rabbits," *Ophthalmic Surg. Lasers* **33**(5), 400–409 (2002).

1. Introduction

Ultrafast lasers are becoming increasingly popular for precise dissection of transparent materials and biological tissues. The most common surgical application of femtosecond lasers is making corneal flaps for LASIK refractive surgery, which largely replaced less precise mechanical microkeratomes. Other prospective ocular applications include cataract surgery [1] and lens softening for presbyopia therapy [2]. In addition to surgery, femtosecond lasers have been used in poration of cell membrane [3] and dissection of cellular organelles [4].

To form a continuous cut with a series of pulses, the rupture zones produced by each pulse should overlap. While this sequential approach allows for cuts of arbitrary three dimensional shapes, extensive dissection is time-consuming. For example, tissue segmentation along multiple surfaces in cataract surgery requires tens of seconds [5]. During this time movements of an eye, even when attached to a suction ring, result in discontinuities of the cutting planes, and thus require additional pulses, or increased energy to compensate for the skipped segments. In addition, residual gas bubbles alter the focusing conditions for subsequent pulses and may further decrease the precision of the method. Therefore, applications that involve deep planar cutting, such as cataract surgery or lens softening, could benefit from a regime that produces dielectric breakdown along a line of 1-2mm in length with a single pulse.

In this study we explore a method of producing optical breakdown within a region with high aspect ratio by focusing a laser beam into a line using a combination of a lens and an axicon. While axicon is known to concentrate incident laser energy within an axially

elongated area [6, 7], a lens shortens this region thus increasing the irradiance and making the system more suitable for microsurgery. Laser focusing with an axicon was recently applied to cell poration [8]. While that study demonstrated that axicon-based system allows for 20 times longer axial distance of successful transfection over the conventional method, no insight into the mechanism of formation of the zone of optical breakdown and therefore no means of control of the interaction zone were provided.

Focusing the laser beam with an axicon alone was also used for micromachining [9]. However, such an approach suffers from highly non-uniform axial intensity distribution, which is usually further degraded by imperfect (rounded) tip of real axicons [10]. Recently a method of focusing laser beam into a high aspect ratio zone with uniform axial intensity distribution has been demonstrated [11]. The method utilizes a spatial light modulator in order to produce non-diffracting Bessel beam and tune the intensity distribution within its focal region. A system operating on this principle was successfully utilized for drilling microchannels in glass samples [12]. Other ways of producing Bessel beams include illumination of annular aperture [13], focusing by a converging lens that has spherical aberration [14], reflecting off of a metal axicon mirror [15], or filtering the incident beam with a binary hologram [16] or a Fabri-Perrot resonator [17].

In the current study we measure aspect ratio of the breakdown zone and demonstrate that its axial location and length can be adjusted by modifying the incident beam profile with an amplitude mask.

2. Experimental setup

An amplified Ti:Sapphire laser system (800nm, 1ps, 1mJ) was operated at 10Hz repetition rate, and single pulses were selected with a mechanical shutter. The laser pulse energy was controlled using a variable attenuator consisting of a combination of a half-wave plate and a polarizing beam splitter. The Gaussian beam was then expanded to $2w = 8\text{mm}$ to efficiently utilize the 10mm diameter aperture of the axicon (refractive index $n = 1.45$, apex angle $\alpha = 179^\circ$) and a 10x microscope objective, NA = 0.3 (Olympus), as diagrammatically shown in Fig. 1a.

The incident beam intensity profile was adjusted by an amplitude mask placed directly (within 3mm) in front of the axicon. The masks were made by printing computer generated 8-bit gray-scale images on a photographic film at resolution 3048 dpi (Chicago Albumen Works). The printouts were negative with respect to the original images, with the maximum and minimum transmission of 60% and 2%. To account for the film nonlinearity its optical density has been measured for a number of digital gray levels prior to mask fabrication. The obtained calibration curve was used to design the masks with a defined optical density profile.

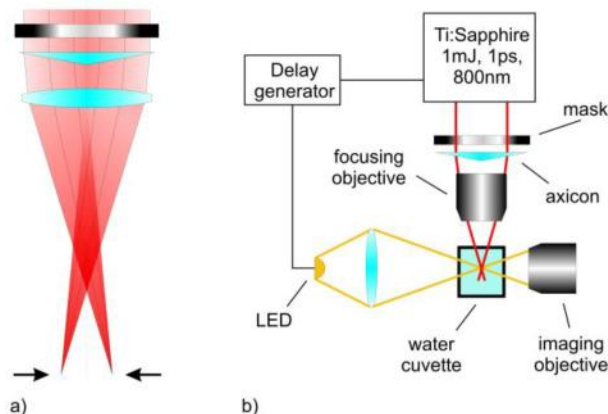


Fig. 1. a) Diagram of the focusing system including an axicon and a lens. Focal plane of the lens is indicated by two arrows. Geometrical rays at various radii from the beam center (shown as lines) cross the axis at distinct locations. b) Experimental setup: laser is synchronized with the flash (an LED) with variable delay generator (temporal resolution 100ns).

Cavitation bubbles were observed in distilled water using fast-flash photography (Fig. 1b). The images were acquired by a custom made microscope consisting of a 10x objective (Nikon, NA = 0.3), 250mm field lens, and a CCD camera (Photometrics CoolSnapHQ). Water was held in a cuvette made of thin (0.17mm) coverslips, and bubbles were generated near the cuvette wall to allow for high resolution imaging through a thin layer of material. The illumination was provided by an LED (OptoDiode Corp., OD-620L) focused onto the sample by a lens matching the NA of the imaging objective. Flashes of 100ns duration were produced by driving the LED with short pulses from a pulse generator. Owing to high reproducibility of bubble behavior, different moments of bubble evolution were captured by varying the delay between the flash and the laser pulse.

3. Results

3.1 Breakdown region with high aspect ratio

Laser intensity distribution in the focal area has been visualized using 2-photon fluorescence of the fluorescein added to the cuvette, which produced signal proportional to the laser intensity squared (Fig. 2). As expected, an elongated region of high light intensity was visible along the axis of the beam before the focal plane of the objective. At sufficiently high laser energy plasma was visible in a part of that region (indicated by inclined arrow).

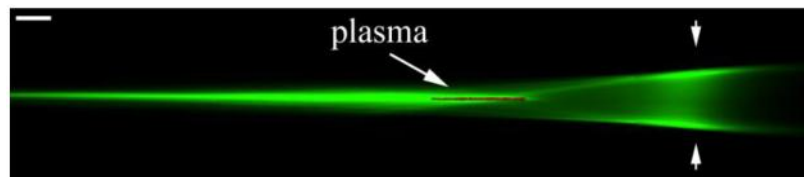


Fig. 2. Intensity distribution within the breakdown region visualized by two-photon fluorescence (green false-color) with overlaid plasma (red false-color, indicated by inclined arrow). Vertical arrows mark the location of the focal plane of the lens. Scale bar represents 100 μ m. Laser beam is incident from the left.

In contrast to conventional lens, that focuses laser beam into a compact ellipsoidal zone of $1.22\lambda/\text{NA}$ in width and $4\lambda/\text{NA}^2$ in length [18], a combination of an axicon and a lens distributes pulse energy over a much longer area as seen in Fig. 2. Accordingly, the threshold of cavitation bubble formation was much higher with axicon than with just a lens: 14 μ J compared to 0.7 μ J. With increasing pulse energy the initial bubble length increases primarily towards the beam origin, while the position of the distal end remains practically the same, which suggests that axial intensity steadily increases with distance from the axicon and then drops abruptly behind a certain point.

With 65 μ J pulses we obtained bubbles of 1.1mm in length and 10 μ m wide 0.1 μ s after the pulse (Fig. 3, top frame). These numbers can be used to set the lower limit on the aspect ratio of the breakdown zone, which is greater than 100:1.

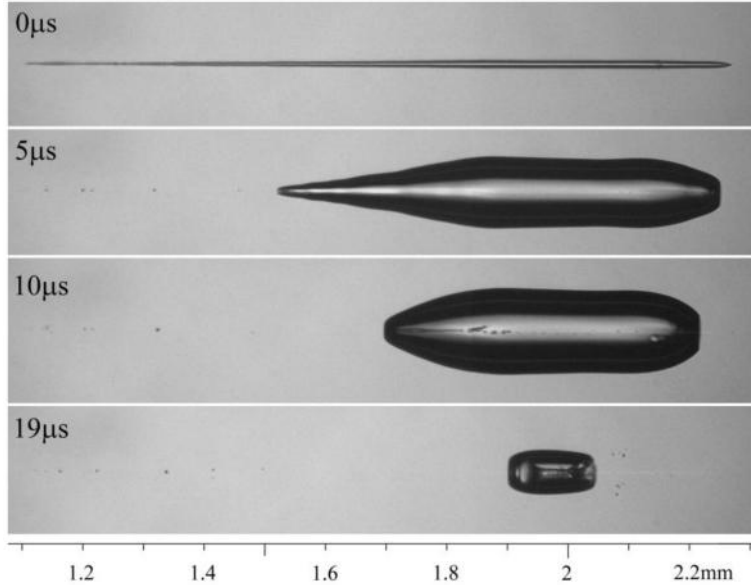


Fig. 3. Evolution of the bubble produced by a pulse of $65\mu\text{J}$. From top to bottom: the frames are taken at less than 0.1 , 5 , 10 , and $19\mu\text{s}$, respectively. The zero of the ruler is located at the water boundary facing the laser beam. The laser is incident from the left.

Being an inviscid and transparent fluid, water is well suited for the analysis of the axial intensity distribution within the breakdown region by examining the dynamics of the produced cavitation bubble. While more detailed studies of the behavior of elongated bubbles can be found in [19–22], here it is important to point out that bubble dynamics allows evaluating uniformity of the axial beam distribution. Intensity variations along the axis result in changes of the maximum bubble width with axial location and different lifetime of the bubble segments – both effects observable with a shadow flash photography. Figure 3 shows non-uniform expansion and collapse of the bubble due to uneven energy distribution along the axis of the breakdown region. The distal part of the bubble, which is produced at higher irradiance, is wider, and therefore has longer radial oscillation time – several microseconds, while the proximal end collapses within a microsecond [23].

3.2 Controlling position of the breakdown region with a disk-shaped mask

Simple ray tracing, schematically shown in Fig. 1a, illustrates that concentric rings of the incident beam are concentrated by an axicon-lens combination in different points along the axis, unlike a lens that would focus all the rings in one point. This feature allows for precise control over the axial location of the breakdown region by blocking certain portions of the incident beam. This approach was tested with disk-shaped masks represented by an opaque circle on a transparent background. As shown in Fig. 4, by increasing the radius of the blocked portion R_{disk} from 1.5mm to 3mm , the location of the proximal end of the bubble was shifted from 1.6mm to 2.1mm , counting from the coverslip-water boundary. Note that the position of the distal part of the bubble ($\sim 2.25\text{mm}$ away from that boundary) is not affected by the presence of such mask. Similarly, a mask consisting of a transparent opening on an opaque background allows for affecting the distal part, without influence on the proximal end.

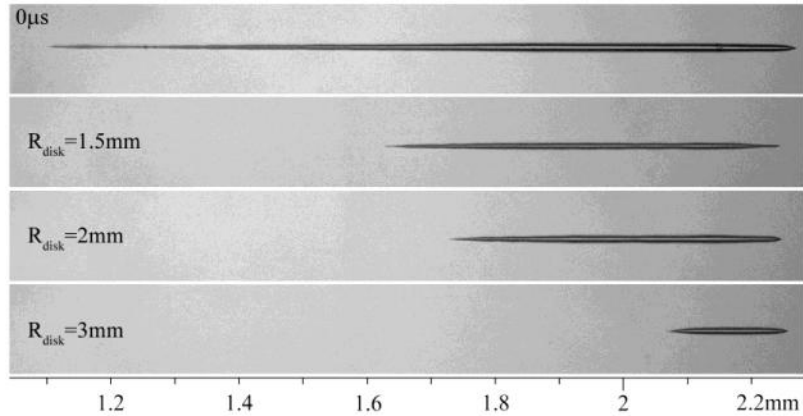


Fig. 4. Effect of “disk-shaped” mask of various radii R_{disk} on the location of the proximal end of the bubble. From top to bottom: bubble without a mask, $R_{\text{disk}} = 1.5\text{mm}$, 2mm , 3mm , respectively. Note that the mask does not affect the location of the distal end of the bubble. All frames are captured within less than 100ns after the laser pulse.

In contrast to longer bubble obtained without a mask, collapse of the bubbles created with the disk-shaped mask is more symmetrical, with both distal and proximal ends imploding towards the midpoint of the bubble, as exemplified in Fig. 5 for $R_{\text{disk}} = 1.5\text{mm}$. Masking the central part of the beam limits the breakdown to the region with relatively uniform axial beam intensity.

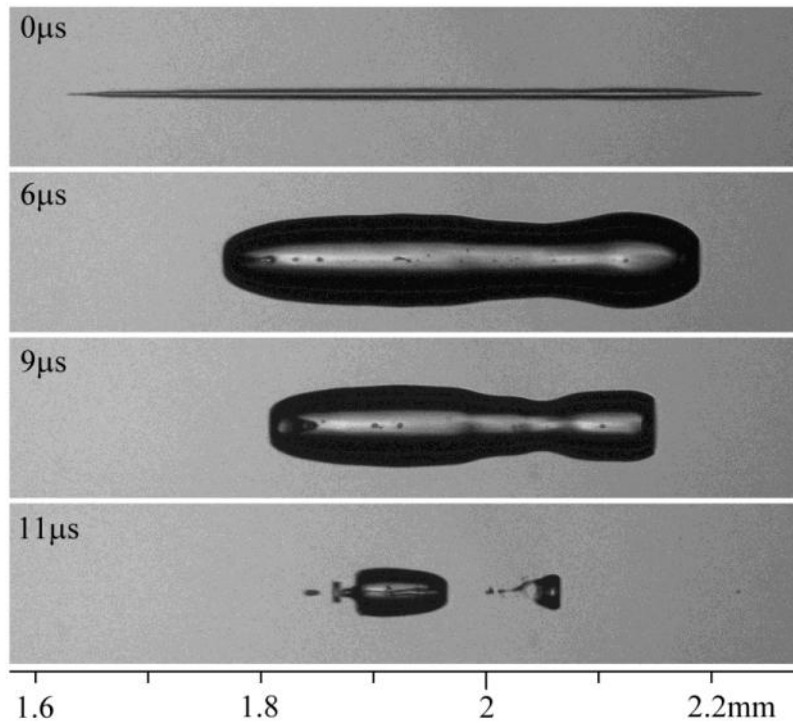


Fig. 5. Dynamics of a bubble produced with a mask of $R_{\text{disk}} = 1.5\text{mm}$. From top to bottom the frames are acquired at: less than 100ns, $6\mu\text{s}$, $9\mu\text{s}$, and $11\mu\text{s}$ after the laser pulse.

3.3 Optimization of the axial intensity distribution with a gradient mask

To produce a uniform cylindrical bubble over the entire breakdown region requires uniform laser fluence distribution along the optical axis in the focal area. This could be accomplished by appropriately tailoring radial intensity distribution of the beam at the input of the axicon-lens system using a mask. To analyze fluence distribution in the focal area and to design appropriate transmission mask we used Fresnel approximation. Accordingly, the energy fluence in a Gaussian beam passing through the axicon and a perfect lens can be described as [24]:

$$I(\rho, z) = \frac{2E}{\pi w^2} \frac{k^2}{z^2} \left| \int_0^R \exp \left[-\frac{r^2}{w^2} - ik \left(r \sin \theta + \frac{r^2}{2f} - \frac{r^2}{2z} \right) \right] J_0 \left(\frac{kr\rho}{z} \right) r dr \right|^2 \quad (1)$$

Here ρ and z are cylindrical coordinates of a point of interest with origin set at the plane of the lens, E is the pulse energy, w is the beam waist, k is the magnitude of the wave vector, R is the radius of clear aperture of the axicon, θ is the angle of refraction produced by the axicon, f is the focal length of the lens, and $J_0(x)$ is the zero order Bessel function. To account for presence of water the nominal focal length f_{lens} was replaced with the effective focal length:

$$f = d_{air} + n_w (f_{lens} - d_{air}) \quad (2)$$

where d_{air} is the distance from the lens to the water surface, n_w is the refractive index of water.

We have computed numerically the integral for the laser beam parameters used in the experiment, and found fluence on the axis ($\rho = 0$), shown in Fig. 6a.

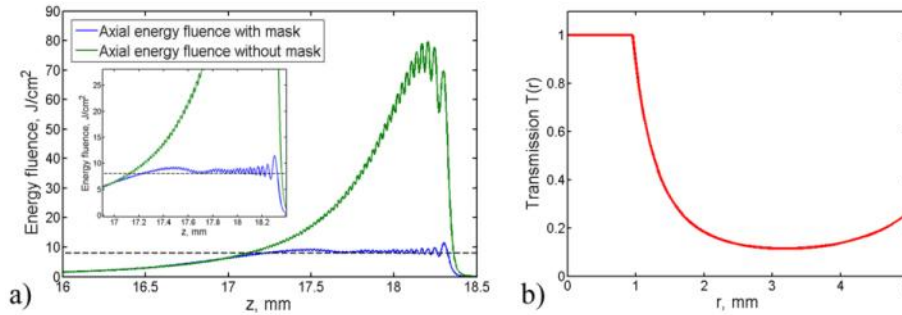


Fig. 6. a) Axial fluence distribution without (green) and with (blue) the “gradient” mask. Dashed line indicates the dielectric breakdown threshold. Pulse energy of $65\mu\text{J}$ was used for calculations; b) “Gradient” mask intensity transmission profile.

In agreement with our experimental observations, laser fluence slowly increases with distance from the lens, followed by an abrupt drop near the focal plane. These calculations together with experimental observations of the cavitation bubble have been used to determine laser breakdown threshold. We applied two methods to find its value. The first one was based on creating a long breakdown region using the full laser energy of $65\mu\text{J}$, finding location of its proximal end, and calculating fluence at this location substituting laser energy into the Fresnel integral. This method yields value of the breakdown threshold of $\sim 8\text{J}/\text{cm}^2$. The second method was based on finding minimal laser energy sufficient to generate breakdown at the top of the intensity distribution. Minimal laser energy, determined as a threshold of bubble formation, was found to be $14\mu\text{J}$. This method yields the breakdown threshold of $17.2\text{J}/\text{cm}^2$. The discrepancy can be associated with inaccuracy in determination of the location of bubble ends in the first method, with the difficulty in imaging cavitation bubbles produced by near-threshold pulse in the second approach [25], and with non-linear effects such as self-focusing and plasma filamentation at high pulse energy, which are not taken into account in the Fresnel integral calculation. The measured threshold for a spherical bubble (without an axicon) was

16.8J/cm² which is in a good agreement with the threshold for axicon and is similar to the published data [26–29].

Note that the axial fluence produced by the axicon and lens varies by a factor of ~10 over the breakdown region, leading to significant widening of the distal end of the bubble, as observed in the experiment.

Transmission mask that modifies incident Gaussian beam and produces more uniform axial intensity distribution can be designed either by examining the integral in Eq. (1) or, much simpler, by applying the stationary-phase analysis [30]. In order to calculate the axial intensity using this approach we need to know the phase ψ and the corresponding radial stationary point ρ_c :

$$\psi(r, z) = \frac{r^2}{2z} - r \sin \theta - \frac{r^2}{2f} \quad (3)$$

$$\rho_c = \frac{fz \sin \theta}{f - z} \quad (4)$$

For the field amplitude transmission function $t(r)$ of the mask (related to the intensity transmission function $T(r) = t^2(r)$), the axial intensity distribution becomes [30]:

$$\begin{aligned} I_{axial}(z) &= \frac{2E}{\pi w^2} \frac{k^2}{z^2} \exp(-2\rho_c^2/w^2) \left[\frac{2\pi}{k\psi^{(2)}(\rho_c, z)} \right] \rho_c^2 T(\rho_c) \\ &= \frac{4E}{w^2} \frac{kz f^3 \sin^2 \theta}{(f - z)^3} \exp\left[-\frac{2(fz \sin \theta)^2}{w^2(f - z)^2}\right] T\left(\frac{fz \sin \theta}{f - z}\right). \end{aligned} \quad (5)$$

Since the incident energy at every radial position is focused into its own location on the axis, the breakdown is formed by an annular part of the beam between radii r_{\min} and R where the value of r_{\min} defines the position of the proximal end of the breakdown zone. In our case the coordinate of the proximal end $z = 16.6$ mm, which corresponds to $r_{\min} = 0.9$ mm. For $r > r_{\min}$ the amplitude transmission function $T(r)$ is found from (5) by requesting $I_{axial}(z) = const$:

$$T(r) = \left(\frac{r_{\min} + f \sin \theta}{r + f \sin \theta} \right)^2 \frac{r_{\min}}{r} \exp\left[\frac{2r^2}{w^2} - \frac{2r_{\min}^2}{w^2} \right], \quad r_{\min} < r < R, \quad (6)$$

The transmission of the central area of the mask ($r < r_{\min}$) can vary. Making it 100% opaque would minimize the overall sample exposure, however, the sharp edge at $r = r_{\min}$ results in highly oscillatory axial intensity. Making this area transparent, i.e. setting $T(r) = 1$ for $r < r_{\min}$, eliminates such oscillations, but slightly increases the sample exposure. This increase is not significant due to small size of this zone: $(r_{\min}/w)^2 = 0.05$. To further decrease the sample exposure while avoiding oscillations in the focal zone, transmission in this area can be gradually increased with radius from 0 in the center to 1 at r_{\min} .

The intensity transmission function $T(r)$ defined by Eq. (6) is shown in Fig. 6b. Since stationary-phase analysis does not account for aperture edges it was deemed necessary to verify the performance of such mask by direct numerical calculation of the diffraction integral (Fig. 6a, blue curve). The effect of sharp edge of the axicon aperture is indeed present in the form of rapid oscillations of the intensity distribution, and can be in principle minimized by appropriate apodization. The maximum variation of the axial intensity due to the oscillations did not exceed 40% of the breakdown threshold (blue line in Fig. 6a) – much less than the factor of 10 that was obtained with the original (unmasked) beam (green line in Fig. 6a).

To evaluate the width of the breakdown zone we calculated radial intensity distribution in the focal area close to the region of maximum intensity (Fig. 7). This intensity distribution consists of the strong central peak with full width at half-maximum (FWHM) of ~2 μ m and side lobes, which do not exceed ~15% of the central peak intensity. Since transmission mask allows one to keep intensity variations along the breakdown region within 40%, the width of

the breakdown region in the masked beam is limited to the $\sim 2\mu\text{m}$ wide central peak. Therefore, the aspect ratio of the breakdown zone (of length 1.1mm) is $\sim 550:1$. A Gaussian beam with the same FWHM would have confocal parameter of $\sim 23\mu\text{m}$, and produce breakdown zone of the similar length. This length is almost a factor of 50 shorter than the length of the breakdown zone achieved with the beam produced by an axicon-lens combination.

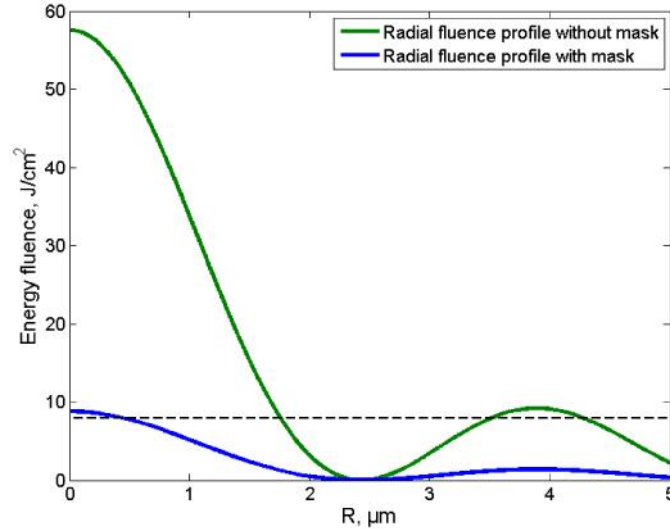


Fig. 7. Radial fluence profile calculated by formula (1) at $z = 18\text{mm}$ without (green) and with the mask (blue). Dashed line indicates the estimated breakdown threshold of $8\text{J}/\text{cm}^2$.

We have tested the computed mask profile experimentally and found that resulting cavitation bubble had the same axial extent but much more uniform width over its length, compared to the unmasked system (Fig. 8). Laser pulse energy in front of the mask was $270\mu\text{J}$, corresponding to $65\mu\text{J}$ transmitted to the sample. This result demonstrates improvement in uniformity of the axial intensity distribution using gradient mask. Taking into account transmission of the clear film (0.6), our theoretical estimate of the pulse energy for the bubble of 1.1mm length was $65/0.6 = 108\mu\text{J}$, whereas higher value ($270\mu\text{J}$) was obtained experimentally. This discrepancy may be attributed to several factors. Deviation of the laser beam profile from Gaussian, especially in the periphery where most of the mask modulation is applied, may increase the breakdown threshold. Theoretical estimates also did not account for nonlinear beam propagation, such as self-focusing and plasma filamentation, which could occur in the focal zone.

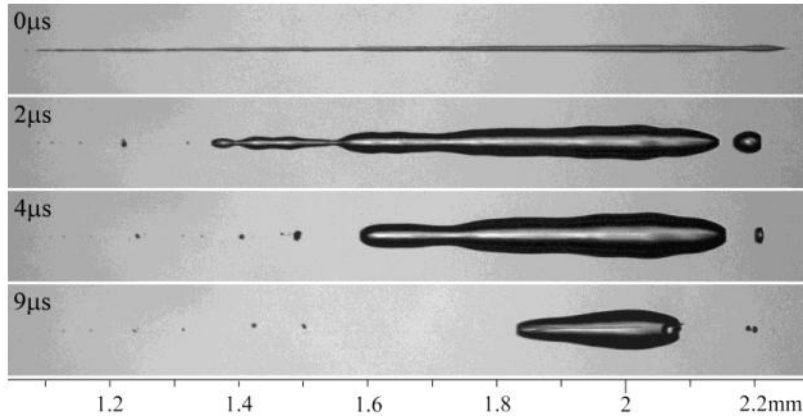


Fig. 8. Dynamics of a bubble produced with the “gradient” mask at less than 100ns, 2 μ s, 4 μ s, and 9 μ s after the laser pulse. Compared to the unmasked beam, this bubble is narrower, more uniform, and has shorter lifetime.

Beam profile can be modified using an electronic spatial light modulator (e.g. LC-R, HOLOEYE Photonics AG, Berlin, Germany), allowing for better control over the actual mask transmission [31]. The fast (a few milliseconds) response time of such modulators provides an opportunity to adjust them between laser pulses, based on a feedback system, which could facilitate more exact control of the shape and the size of the breakdown region.

Inherent drawback of the amplitude beam profile modulation is the energy loss, which might be a substantial obstacle for practical implementation of such a system. The phase modulation of the laser beam might be an ultimate solution for creating adjustable breakdown region in the transparent material.

3.4 Energy considerations – cutting efficiency and safety limitations

In sequential cutting with spherical bubbles the spot spacing is typically on the order of a bubble radius R_b [32], and thus the number of bubbles required for such a cut $N = L/R_b$. For example, for $R = 25\mu\text{m}$ and $L = 1.1\text{ mm}$, $N = 44$. The total volume of these bubbles $V = 4/3\pi R^2 * L$ is similar to that of a cylinder with the same radius R_b and length L : $V = \pi R^2 * L$. Therefore, the total amount of energy required for cutting a line with a series of spherical bubbles and with a single cylindrical bubble of the same radius are similar (assuming the same energy conversion efficiency for the cylindrical and spherical bubbles).

In ophthalmic applications part of the laser energy that is not absorbed in the focal zone contributes to heating of the retina. If 67 μJ is focused into human crystalline lens at $\text{NA} = 0.1$, it produces retinal radiant exposure of approximately 800 $\mu\text{J}/\text{cm}^2$ – over two orders of magnitude below the fluence at which retina pigment epithelium cells get damaged by explosive vaporization of melanosomes – 100 mJ/cm^2 [33–35]. However, to limit the average retinal heating during prolonged exposure by the same level as with a sequential approach, the laser power should be restricted to the same value, and the pulse repetition rate needs to be reduced accordingly. Therefore cutting planar patterns with the same average laser power will result in the same total duration of the procedure, whereas significant gain in speed can be achieved when creating line cuts (e.g. in applications to membrane poration). For both planar and line cutting the main advantage of the proposed approach is the ability to produce almost instantaneous (within the pulse duration) axial incision without scanning.

4. Conclusions

We have demonstrated highly elongated optical breakdown in water with aspect ratio over 550:1 by focusing laser beam with a combination of an axicon and a lens. Modifying radial intensity distribution of the incident laser beam with the amplitude masks improved homogeneity of the 1mm long linear breakdown zone and allowed for controlling its length

and axial position with 0.1mm accuracy. Axial homogeneity has been improved by a factor of 7, compared to unmasked beam, and did not exceed variation of 40% along the 1.1 mm length of the breakdown zone. Electronic amplitude and phase spatial light modulators may allow for further perfection of the beam profile and for adjustment of the axial position of the dielectric breakdown zone without moving optical elements.

Acknowledgment

This work was supported by U. S. Air Force Office of Scientific Research (AFOSR) (grant FA9550-04-1-0075).